Journal of Electron Spectroscopy and Related Phenomena 283 (2025) 147575

Contents lists available at ScienceDirect

Journal of Electron Spectroscopy and Related Phenomena

journal homepage: www.elsevier.com/locate/elspec

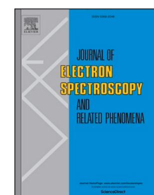

Experimental electron band alignment of 1T'and 2H $MoTe_2/SiO_2$ interface using internal photoemission spectroscopy

Pinaka Pani Tummala [a,b], Valeri Afanas'ev [c,e], Gabriele Ferrini [d], Mario Alia [a], Andrea Serafini [f], Paolo Targa [f], Davide Codegoni [f], Christian Martella [a], Alessandro Molle [a], Alessio Lamperti [a,*]

[a] CNR IMM, Unit of Agrate Brianza, via C. Olivetti 2, Agrate Brianza 20864, Italy
[b] Institute for Functional Intelligent Materials, National University of Singapore, Singapore 117544, Singapore
[c] Department of Physics and Astronomy, Katholieke Universiteit Leuven, Celestijnenlaan 200D, Leuven B-3001, Belgium
[d] Interdisciplinary Laboratories for Advanced Materials Physics (I-LAMP), Dipartimento di Matematica e Fisica, Università Cattolica del Sacro Cuore, via della Garzetta 48, Brescia 25133, Italy
[e] IMEC, Kapeeldreef 75, Leuven B-3001, Belgium
[f] STMicroelectronics, Via C. Olivetti 2, Agrate Brianza I-20864, Italy

ARTICLE INFO

Keywords:
Two-dimensional materials
Molybdenum ditelluride
Band alignment
Energy band structure
Phase engineering
Internal photemission spectroscopy

ABSTRACT

Unlike other two-dimensional (2D) transition metal dichalcogenides, molybdenum ditelluride ($MoTe_2$) displays a stable biphasic character in artificially synthesizable 2H and 1T' state. While these phases are inherently distinguished in their electronic band character (semiconducting and metallic, respectively), it is not clear how they electronically interface with technology relevant substrate where to engineer an electronic device layout. In this study, we experimentally determine the electron band alignment at interfaces between SiO_2 and 1T'/2H of $MoTe_2$ few-layers ultrathin films grown by chemical vapor deposition. We use internal photoemission spectroscopy to determine the energy barrier height between the 1T'/2H-$MoTe_2$ Fermi level and the oxide conduction band (CB) bottom. This observation indicates the band gap opening in 2H-$MoTe_2$ and provides an estimate of the barrier height for holes at the polytypic 1T'/2H-$MoTe_2$ interface. In particular, by comparing the Fermi level energy in single-phase 1 T'-$MoTe_2$ with the VB energy in 2H-$MoTe_2$, we reveal a ≈ 0.4 eV difference, suggesting that the low Schottky barrier observed at the 1T'/2H interface results from Fermi level pinning, which is independent of interface defects and unaffected by the VdW gap. Our findings can be exploited for optimizing charge transport and device performance, facilitating the development of next-generation electronic and opto-electronic devices that harness the unique properties of both phases in $MoTe_2$.

1. Introduction

In the race of extensive research to continue the size scaling in complementary metal-oxide-semiconductor (CMOS) technology, two-dimensional transition metal dichalcogenides (2D-TMDs) like MoS_2, WS_2 and $MoTe_2$ could compete with the present silicon technology by offering atomically thin channels [1–3]. The versatility of various 2D-TMDs enables them to be arranged in different ways to create a wide range of devices, giving future applications the ability to adjust their physical characteristics by design [4–6]. In this context, molybdenum ditelluride ($MoTe_2$) exhibits distinct metallic and semiconducting phases, which can be interplayed so as to create metal-semiconductor junctions supported by a common SiO_2 substrate on a transistor-like layout. $MoTe_2$ crystallizes into several different structures, namely the hexagonal 2H structure (α-phase), the monoclinic 1T' structure (β-phase), and the low temperature orthorhombic T_d phase [7,8], which have been observed to transform or transition under several conditions [9–13] In the metallic phase, 1T'-$MoTe_2$ possesses an extremely small band gap of up to 60 meV in few layer-thin film and, as the material gets to its bulk state, this small bandgap disappears, as suggested by density functional calculations, thus promising good electrical conductivity as metal contact [7,14]. In its bulk system, 1T' $MoTe_2$ exhibits characteristics of a type II Weyl semimetal when distorted into the orthorhombic T_d phase, which is the only polymorph of $MoTe_2$ that lacks inversion symmetry and can therefore host the Weyl state [11]. In contrast, the monolayer of $MoTe_2$ behaves as a quantum spin Hall insulator. On the

* Corresponding author.
E-mail address: alessio.lamperti@cnr.it (A. Lamperti).

https://doi.org/10.1016/j.elspec.2025.147575
Received 15 July 2025; Received in revised form 24 September 2025; Accepted 30 October 2025
Available online 31 October 2025
0368-2048/© 2025 The Authors. Published by Elsevier B.V. This is an open access article under the CC BY-NC-ND license (http://creativecommons.org/licenses/by-nc-nd/4.0/).

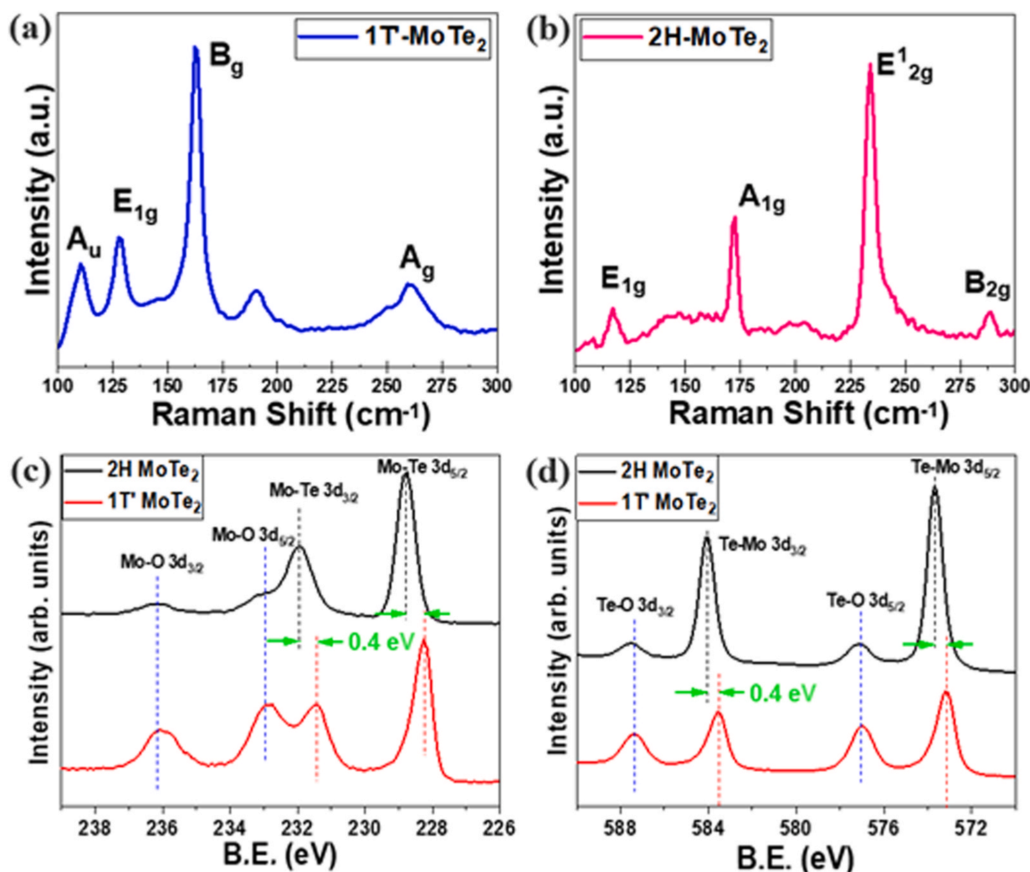

Fig. 1. Raman spectra of the CVD grown of (a) metallic 1T'- $MoTe_2$ (b) semiconducting 2H-$MoTe_2$ (c-d) XPS spectra of Mo 3d and Te 3d core levels of 2H-$MoTe_2$(black line) and 1T'-$MoTe_2$(red line) showing binding energy peaks of Mo ($3d_{3/2}$, $3d_{5/2}$) and Te ($3d_{3/2}$, $3d_{5/2}$) with their corresponding minimal oxidized peaks of Mo-O $3d_{5/2}$,$3d_{3/2}$ and Te-O $3d_{5/2}$,$3d_{3/2}$.

other hand, in the semiconducting phase 2H-$MoTe_2$ is stable at room temperature and displays an indirect band gap of $\geq$ 1 eV in bulk [14–16]. The tunability of the band gap in this phase allows for precise control of the electrical conductivity, making $MoTe_2$ suitable for designing high-performance transistors [17]. In particular, semi-conducting 2H-$MoTe_2$ has gained significant attention in recent years due to its exceptional properties, including high electron mobility, efficient charge transport, and excellent ambipolar characteristics [18, 19]. The latter aspect makes $MoTe_2$ an interesting candidate for next-generation electronic CMOS devices, particularly tunable n- and p-channel field-effect transistors (FETs).

In addition, while 2H-$MoTe_2$ combined with other 2D materials-based tunnel FETs (TFETs) has been considered promising due to its ability to provide a significantly enhanced on-off current ratio within a specific gate voltage swing and lower power consumption, there are still several challenges in its application [20]. These include limitations in accurately quantifying the barrier height at the interfaces between 2D semiconductors and insulators, which is critical for understanding the electrostatics and built-in potentials in an operational transistor layout. Furthermore, although $MoTe_2$, with its p-type characteristics, small band gap, and low electron affinity, is increasingly utilized in electronic and optoelectronic fields such as tunnelling FETs [18], photovoltaic detectors [21], light-emitting devices, and memory devices [20], its integration with other 2D materials like MoS_2 (which demonstrates n-type characteristics and high electron affinity) in heterostructures requires a deeper understanding of the interface properties [4,22,23]. The challenges surrounding the energy barrier at the 2D-2D interfaces hinder the performance and scaling of these devices. In this context, the conducted internal photoemission spectroscopy studies may offer valuable insights into these interface properties, providing potential solutions to quantify the barrier height accurately and enable the development of transistor technologies with effective field modulation and very steep sub-threshold slopes, crucial for low-voltage electronics [14,22,24]. On the other hand, disclosing the band line-up between 1T'-$MoTe_2$ and an insulating layer is useful to disclose the emergence of electrical dipoles which can be related to Fermi level pinning in the resulting Schottky junction.

Starting from well-identified 2H and 1T' $MoTe_2$ films, we experimentally deduced the band alignment at the SiO_2 interface using internal photoemission of electrons (IPE) spectroscopy from the $MoTe_2$ valence state. In all cases, $MoTe_2$ was directly CVD grown as few-monolayer thin metallic 1T'-$MoTe_2$ and semiconducting 2H-$MoTe_2$. Using IPE, we were able to determine the energy position of the Fermi level of metallic 1T'-$MoTe_2$ as well as the semiconductor (2H-$MoTe_2$) valence band (VB) relative to the refence level of the insulator (SiO_2) conduction band (CB).

In polytype-controlled contacts, where chemical intermixing or contamination is excluded, we can explore a more fundamental question regarding the alignment of the Fermi level in 1T'-$MoTe_2$ and the valence band (VB) maximum in 2H-$MoTe_2$ which can be of relevance for contact engineering in TMD transistor channel [25–27]. Specifically, we may wonder whether the electron states of the same type govern both energies, or if the Fermi level is "pinned" at the homojunctions despite the presumed lack of coordination defects (such as dangling bonds) and the presence of a van der Waals (VdW) gap in the vertical contacts. In both cases defects cannot be responsible for the violation of charge neutrality at the polytypic homojunction. In this study, we compare the Fermi level energy in single-phase 1T'-$MoTe_2$ with the VB energy in 2H-$MoTe_2$ measured with respect to the common reference energy level of the SiO_2 CB bottom edge, revealing a $\approx$ 0.4 eV difference between the two. This

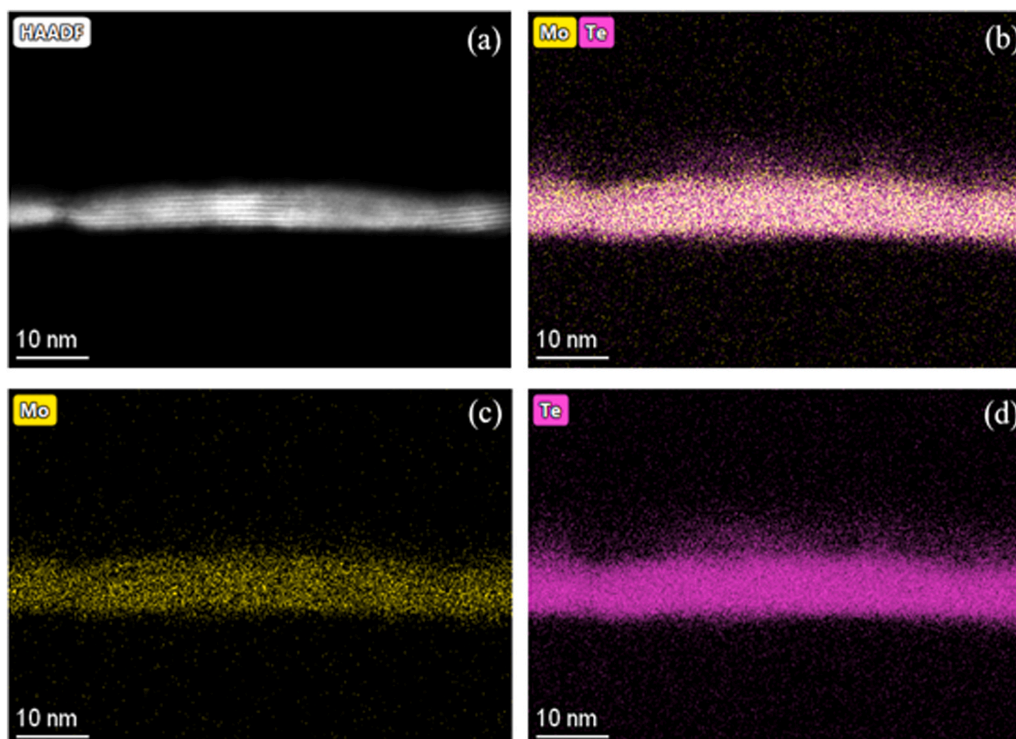

Fig. 2. (a) Cross sectional TEM image of CVD grown $MoTe_2$ along with EDX elemental mapping (b) $MoTe_2$ (c) molybdenum and (d) tellurium.

finding suggests that the low Schottky barrier observed at the 1T'/2H interface results from Fermi level pinning, which is independent of interface defects and unaffected by the VdW gap. This "pinning" effect is likely caused by the electron density tailing of the $MoTe_2$ polytypes extending through the van der Waals gap or across the homojunction interface.

2. Results and discussions

The Raman spectra shown in Fig. 1(a, b), were acquired on the as-grown $MoTe_2$ samples with lateral dimensions of 3 cm × 1 cm (sample images shown in Figure SI 3). Fig. 1(a) reveals the existence of phonon modes located at 108, 127, 257, and 163 cm^{-1} that are attributed to the A_u, E_{1g}, A_g of out-of-plane, and B_g in-plane phonon vibrational modes, respectively, of the metallic 1T'-$MoTe_2$ phase. The obtained Raman spectra, characterized by distinctive Raman peaks, confirm the presence of pure 1T' phase $MoTe_2$ that are in agreement with literature reports [28–30]. By contrast, the Raman spectra shown in Fig. 1(b) indicate the peaks located at 232 and 291 cm^{-1}, corresponding to the E^1_{2g} and B_{2g} in-plane phonon modes, along with the 118 and 172 cm^{-1} representing the E_{1g} and A_{1g} out-of-plane phonon modes for semiconducting 2H-$MoTe_2$, respectively. These findings are supported by comparison with the typical Raman features observed in mechanically exfoliated flakes of 1T' and 2H - $MoTe_2$ phase in the same allotropic form [28].

The XPS spectra of the large area CVD grown 2H- and 1T′-$MoTe_2$ films confirm the presence of Mo and Te as shown in the Fig. 1(c), (d). Considering the high-resolution XPS peaks of 1T'-$MoTe_2$, the binding energies are centered at 228.3 eV (Mo-Te $3d_{5/2}$) and 573.2 eV (Te-Mo $3d_{5/2}$) respectively, while the corresponding peaks of 2H-$MoTe_2$ are centered at 228.7 eV and 573.6 eV, with a noticeable red-shift by about 0.4 eV, consistent with the previous reports on exfoliated crystal [31]. These differences in binding energies were attributed to the different lattice symmetry in the two phases [31]. In addition, the weak shoulder peaks of Mo−O $3d_{5/2}$ at 233.2 eV, Te−O $3d_{5/2}$ at 577.4 eV, Mo−O $3d_{3/2}$ at 236.3 eV, and Te−O $3d_{3/2}$ at 587.1 eV are observed in both 1T' and 2H-$MoTe_2$, which may result from oxidation during sample handling and transfer. It is worth mentioning that in metastable phase of 1T'-$MoTe_2$, the intense oxides peaks were observed indicating rapid oxidation in 1T'-$MoTe_2$ compared to 2H-$MoTe_2$ due to the presence of dense Te vacancies in 1T'-$MoTe_2$ compared to 2H-$MoTe_2$ as seen in the red spectra in Fig. 1(c), (d) [32].

The elemental composition of $MoTe_2$, grown on SiO_2/p^+-Si substrates, can be determined by using energy-dispersive X-ray spectroscopy (EDX) maps as shown in Fig. 2. This analysis was performed using transmission electron microscopy (TEM) in high-angle annular dark field (HAADF) mode, which has a high sensitivity to the atomic number Z. Fig. 2(a) shows cross-sectional TEM image of the direct tellurized $MoTe_2$ film representing the layer-by-layer structure. The thickness of as-grown $MoTe_2$ film is around ~ 8 nm, revealing the continuous growth with typical layered structure of $MoTe_2$. Fig. 2(b-d) presents the same area examined using EDX for elemental mapping. The elemental maps in Fig. 2(b), (c), and (d) confirm the presence of a continuous layer of $MoTe_2$ and reveal the spatial distribution of Mo and Te atoms. The EDX spectrum in Fig. 2(d) provides clear evidence of a high atomic ratio density, indicating tellurium enrichment. TEM was conducted only on 1T' $MoTe_2$ film since the $MoTe_2$ from 1T' and 2H samples were grown using same thickness Mo films.

We analysed the IPE spectra of 10 ML 1T' and 2H-$MoTe_2$ films synthesized under ambient pressure conditions using tellurization of e-beam deposited Mo film in a CVD reactor. During the growth, the phase change from metallic(1T') to semiconductor(2 H) was demonstrated. By conducting IPE investigations, we were able to evaluate the band alignment of both 1T' and 2H-$MoTe_2$ films and determine the position of the VB top edge of $MoTe_2$ relative to the CB of the SiO_2 collector layer. The IPE yield spectra, measured on samples with 10 ML metallic 1T' and semiconducting 2H-$MoTe_2$ films using semi-transparent Au pads, are shown in Fig. 3(a) and (b) as $Y^{1/3} - h\nu$ plots under applied negative bias between the top Au contact and the bottom Al, respectively. These plots were used to determine the spectral thresholds of IPE. The quantum yield of IPE increases with photon energy as $Y(h\nu) \propto (h\nu - \Phi e)^3$, which corresponds to the observed linear increase in yield shown in panels 3(a)

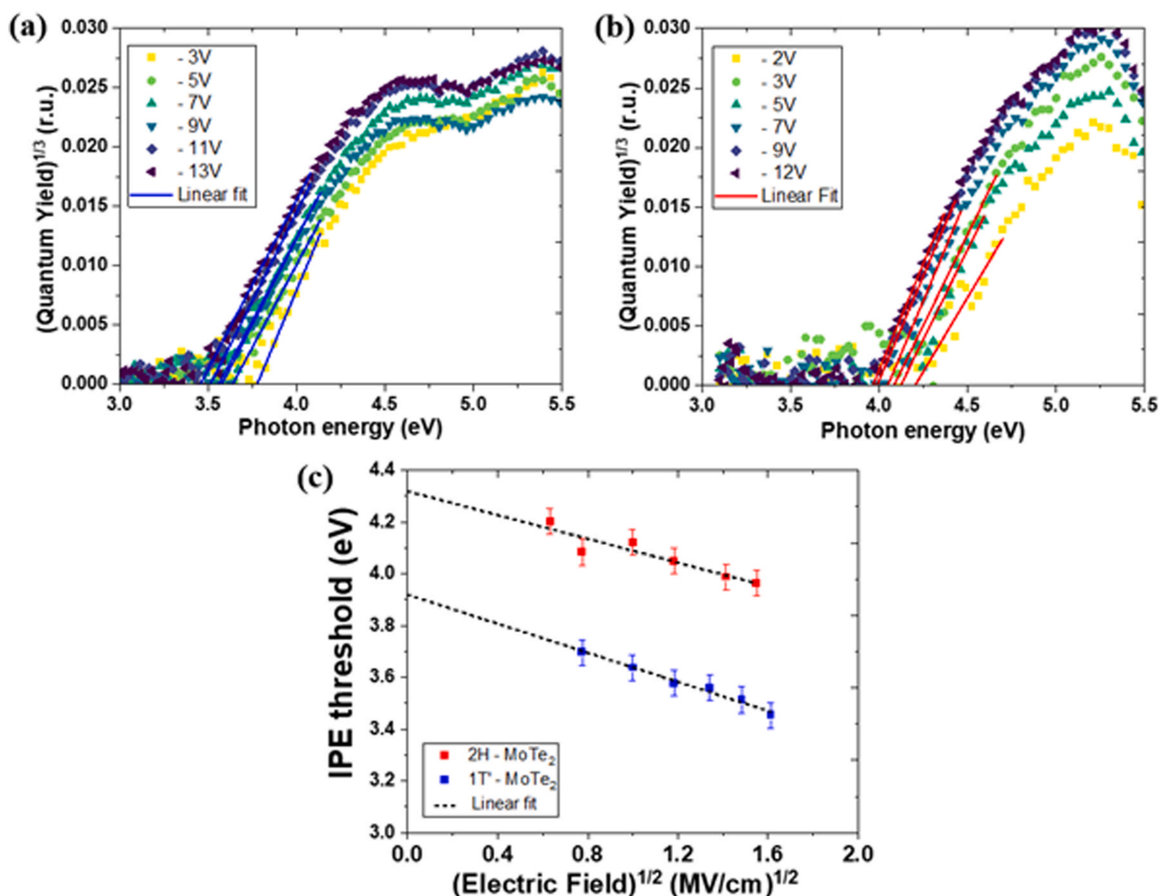

Fig. 3. Powell plots of the IPE quantum yield spectra for CVD grown 10 layers (a) 1T'-$MoTe_2$ and (b) 2H-$MoTe_2$ films under the negative gate biases ranging between −3 V and −13 V. The quantum yield reduction above 5 eV photon energy is caused by the change in the silicon substrate reflectivity which has a peak at E2 Van Hove singularity (4.4 eV) and, at higher energies, by optical interference in the $MoTe_2/SiO_2$ stack. (c) Schottky plot of the inferred spectral thresholds for CVD grown $MoTe_2$. Solid blue lines (panel a) and red lines (panel b) indicate the linear fit used to determine the zero field threshold of corresponding panels (a) and (b).

and (b) [33]. The yield spectrum was measured on a capacitor fabricated by evaporating semi-transparent (15 nm) Au electrodes of 0.5 mm^2 area on top of the same p$^+$-Si/SiO_2(50 nm) substrate (shown in Figure SI 3). Similar results were obtained when using non-transparent Au contact pads enabling observation of electron IPE from un-metallizezd $MoTe_2$ and when using Al as a contact metal instead of Au. These observations indicate $MoTe_2$ as the sole source of electrons contributing to IPE. The spectral thresholds of electron IPE were determined by extrapolating the

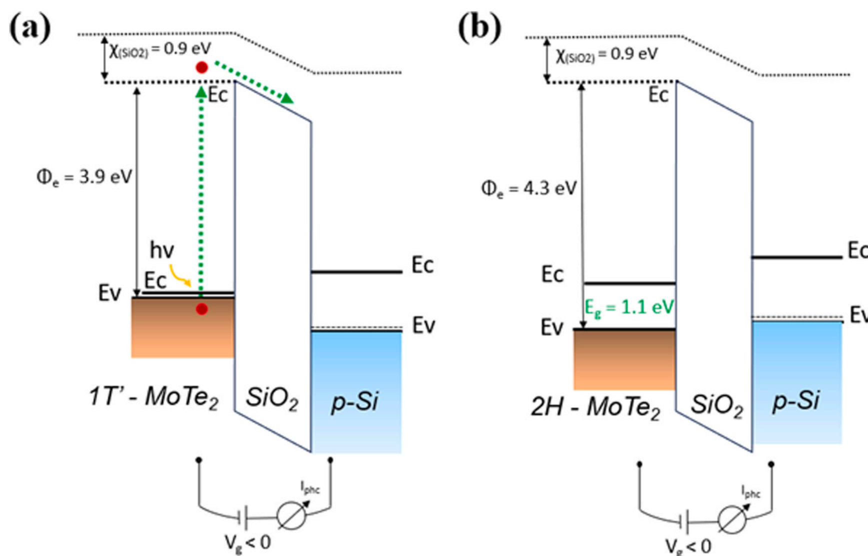

Fig. 4. The energy band alignment diagram showing transport of photoexcited electrons from the valence band (VB) at gating conditions of (a) metallic 1T'-$MoTe_2/SiO_2$/Si (b) semiconducting 2H-$MoTe_2/SiO_2$/Si under applied negative bias to the top electrode. Electron affinity of SiO_2 ($\chi_{(SiO2)}$) is indicated for a reference.

$Y^{1/3}$ – hν plots to zero yield and then plotting the inferred threshold values as a function of the electric field in SiO_2. The choice of cube root plot for IPE from semi-metallic 1T'-$MoTe_2$ is related to the proximity of the Fermi level to the valence band edge as can be seen from the band structure calculations [34]. In this case the electron density of states (DoS) increases with energy leading to p = 3 value similar to that in semiconductors [33]. This energy dependent DoS is the common feature in 2D materials: for instance, the electron IPE spectra of graphene (obviously metallic in its conduction behavior) follow the same p = 3 trend over extended range of photon energies [35]. This was done using the Schottky coordinates Φe(F) vs. $\sqrt{F}$, which enabled us to account for field-induced barrier lowering [27,36,37]. The results presented in Fig. 3(a) and (b) for the 10 ML 1T' and 2H-$MoTe_2$ samples with Au contact pads suggest a barrier lowering with an image force dielectric constant i ≈ 2. This value is close to i ≈ n^2, where n = 1.46 is the refractive index of SiO_2, and corresponds to the ideal case of a charge-free interface [35,37,38].

The IPE yield spectra of $MoTe_2$ grown by CVD tellurization synthesis in Fig. 3(a) and 3(b) show a clear difference in spectral thresholds in the $Y^{1/3}$-hν plots (the Powell coordinates, see Ref. [33]). The spectral thresholds extracted by linear fitting of these $Y^{1/3}$-hν plots at different applied voltages are combined in the Schottky plot shown in Fig. 3(c) plotted linearly to the zero-field energy barriers of 3.9 ± 0.1 eV for 1T'-$MoTe_2$ (blue symbols) and 4.3 ± 0.1 eV for 2H-$MoTe_2$ (red symbols) from the VB top edge of $MoTe_2$ to the SiO_2 CB bottom edge, respectively. The VB top in 10 ML semiconducting 2H-$MoTe_2$ lies ≈ 400 meV below the Fermi level of the 10 ML semi-metallic 1T' $MoTe_2$ film as measured with respect to the common reference level of the SiO_2 CB bottom. The experimental accuracy limit can be estimated as ±50 meV on the spectral threshold and ±100 meV on the zero-field barrier value [39,40]. The so observed VB shift between the two $MoTe_2$ phases can be associated with the band gap opening in 2H phase. It is worth mentioning here that in few-layers form, 1T'-$MoTe_2$ has semi metallic nature with slight band overlap near the Fermi level. However, in mechanically exfoliated few-layers 1T'-$MoTe_2$, a bulk gap of 60 meV was observed from optical absorption and transport measurements [14]. The barrier height between the Fermi level and the oxide conduction band bottom was reproducibly to be 4.2–4.3 eV. The observed change of energy position of the VB top edge of $MoTe_2$ below the SiO_2 CB bottom edge indicates experimentally the band gap opening in semiconducting 2H-$MoTe_2$ grown using CVD tellurization.

Fig. 4 shows the scheme of the energy band lineups measured using IPE at the 1T' $MoTe_2/SiO_2$ from Fermi level of $MoTe_2$ emitter to the CB of SiO_2 **(a)** and 2H-$MoTe_2/SiO_2$ from VB top edge of $MoTe_2$ emitter to the CB of SiO_2 **(b)** with SiO_2 interface from 10 ML - $MoTe_2$ synthesized through CVD tellurization from Mo film and tellurium. For phase comparisons, we choose same thickness of 10 ML - $MoTe_2$ in both cases which also provides films with sufficient resistance to oxidation in air as long as IPE measurements repeated after extended air exposure provide identical results as those on the freshly fabricated samples.

The field-dependent IPE measurements (Fig. 3) suggest the $MoTe_2/SiO_2$ interface to be charge-free and, therefore, reflects intrinsic band energies of $MoTe_2$. Then, the observed energy difference between the Fermi level of metallic 1T'- $MoTe_2$ and the VB top of semiconducting 2H-$MoTe_2$ allows us estimate the energy barrier for holes at the 1T'/2H polytypic interface to be ≈ 0.4 eV. This inference provides an interesting solution for contacts to the p-type channel in FET for CMOS applications without need to combine $MoTe_2$ with dissimilar metals. Interestingly, the electron IPE barrier for pure Te on SiO_2 is close to 4.1 eV [31] indicating possibility of barrier tailoring by introducing a Te interlayer between two $MoTe_2$ polytypes. The reported work provides direct information on the energy band alignment of the phase engineered few-layer $MoTe_2$ polytypes as a building block for electronic applications where $MoTe_2$ can be either used as semiconducting channel and contact. Consequently, the nearly zero Schottky barrier heights observed in the polytypic IT'-/2H-$MoTe_2$ contacts arise from the "pinning" of the Fermi level in these homojunction.

3. Conclusion

In conclusion, we employed internal photoemission spectroscopy to investigate the energy band alignment at interfaces of Mo-tellurization synthesized 10 monolayer-thin metallic 1T'- and 2H-$MoTe_2$ films with insulating SiO_2. The transition to 2H-$MoTe_2$ was found to cause a notable energy shift of approximately 0.4 eV in the valence band top edge compared to 1T-$MoTe_2$, indicating the opening of a band gap. Additionally, the nearly zero Schottky barrier heights reported in polytypic 1T'-/2H-$MoTe_2$ contacts are attributed to Fermi level pinning within these polytypic homojunctions. These insights represent a substantial advancement in the development of $MoTe_2$-based electronic devices, offering a deeper understanding of their potential for future applications.

4. Experimental section/methods

4.1. Sample fabrication

Molybdenum ditelluride ($MoTe_2$) was synthesized using a tellurization approach starting with molybdenum films pre-deposited from Mo foil using e-beam evaporation on top of thermally grown SiO_2 layer on Si. The synthesis was carried out in a two-furnace ambient pressure chemical vapor (AP-CVD) apparatus using 50 nm SiO_2/p^+-Si substrates with phase-controlled temperatures. In the AP-CVD reactor, tellurium powder of 100 mg for 1T' (and 200 mg for 2H) were placed in a ceramic boat in the center of the upstream furnace, while the Mo coated substrate was positioned face-up in a closed boat at the starting corner of the downstream furnace. The substrate with the Mo film was tilted inside the closed quartz boat as shown in the Figure SI 1(a). An Ar/4 % H_2 flow was used as carrier gas to transport the Te vapor from the upstream furnace to the downstream furnace, where the heterogeneous vapor-solid reaction with Mo took place to form $MoTe_2$ nanosheets at elevated temperatures. The temperature was ramped controllably from room temperature up to 500 °C in the first 25 min, followed by a plateau maintained for 120 min at 600 and 625 °C for the downstream (Mo) and upstream (Te) furnaces, respectively. The carrier gas flow and temperature profiles used in the AP-CVD process are shown in Figure SI 1, with the temperature profile shown by black line for the upstream (Te) furnace and red line for the downstream (Mo) furnace. The temperature profile followed natural cooling down to room temperature as shown in Figure SI 1(b). The surface morphology of the grown 1T' and 2H-$MoTe_2$ film thickness, extracted from line scan profile, from atomic force microscopy (AFM) were shown in Figure SI 2. A more detailed morphological characterization can be found elsewhere [30].

4.2. Structural and chemical characterization

$MoTe_2$ samples were characterized using Raman spectroscopy, X-ray photoelectron spectroscopy (XPS), and transmission electron microscopy (TEM). Raman spectroscopy was carried out with a Renishaw InVia spectrometer, equipped with a solid-state laser with an excitation wavelength of 514 nm (2.41 eV) in a backscattering configuration. The laser was focused onto the sample using a 50× Leica objective (0.75 numerical aperture), and the incident power was kept below 1 mW to prevent sample damage. XPS measurements were conducted with a PHI ESCA 5600 system, featuring a monochromatic Al Kα x-ray source (1486.6 eV) and a concentric hemispherical analyzer. The spectra were recorded at a 45° take-off angle and with a 23.50 eV band-pass energy, achieving an instrument resolution of 0.5 eV. The spectra were referenced to the C 1 s peak at 285 eV. High-resolution TEM imaging was performed for the microstructural characterization, while the chemical properties of the samples were investigated by TEM energy-dispersive x-ray spectroscopy (EDX). TEM and EDX analyses were conducted on

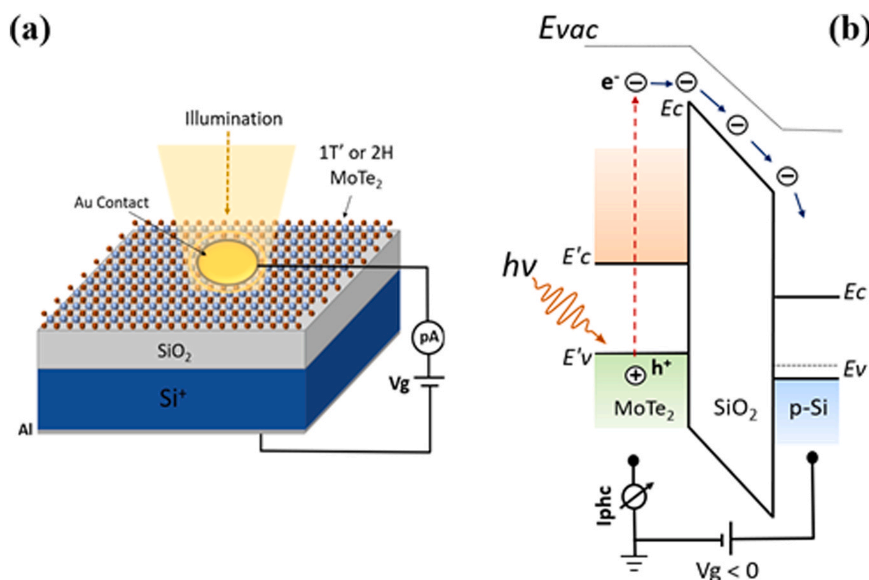

Fig. 5. (a) Schematic of IPE measurements on a 1T' or/and 2H-$MoTe_2/SiO_2/p^+$-Si capacitor with an Au contact pad. The negative bias voltage (Vg) is applied between the Au pad and the back Al contact. (b). Simplified band diagram of the $MoTe_2/SiO_2$(50 nm)/p^+-Si capacitor under negative (Vg< 0).

electron-transparent lamella obtained using focused ion beam (FIB) thinning of cross-section TEM lamellae. The lamellae preparation was performed using a Thermofisher Helios G5UX FIB. Particular attention was taken to limit the heating and ballistic effects of ion irradiation on the samples during the final ion milling steps. This has been done in the lamella preparation by reducing currents and energies progressively from a value of 30 keV to a value of low keV in order to avoid material amorphization and damage. The TEM images were carried out using a Thermo-Fisher Themis Z G3 aberration-corrected transmission electron microscope, equipped with an electron gun monochromator and operating at an acceleration voltage of 200 kV, with scanning TEM (STEM) techniques used to investigate the lamellae.

4.3. Internal photoemission measurements

IPE measurements were conducted at room temperature using a Keithley 6517 A electrometer and monochromatized light from a 150 W Xe arc lamp. The spectral system has a constant spectral resolution of 2 nm and covered the photon energy range hν = 2–6 eV. IPE represents the process in which electrons are excited from occupied states in the VB within an emitter material and are then emitted across the interface into unoccupied states within the CB of a collector material (SiO_2 in our case). This process becomes possible when the energy of photons becomes larger than the energy barrier for electrons ($hv > \Phi_e$) at the interface. Once this condition is met, charge injection into the oxide material takes place, which can be observed through photocurrent measurements. The IPE measurement setup on a capacitor device is schematically shown in Fig. 5(a). Band diagram illustrating the IPE process under the applied negative bias shown in Fig. 5(b). The photocurrent (I_{ph}) was determined by subtracting the dark current from the current measured under illumination and then normalized to the incident photon flux to calculate the IPE quantum yield (Y). Extensive signal averaging was performed to enhance the signal to noise ratio. The power function was used to approximate the yield spectral curves in the photon energy range above the spectral threshold of IPE $h\nu > \Phi e$ [33,36].

$$Y(hv) = A(hv) \bullet (hv - \Phi e)^{p} \quad (1)$$

where the value of A(hv) is determined by the optical properties of the sample and is assumed to remain nearly constant in the narrow range of photon energies near the spectral threshold. The IPE threshold Φe corresponds to the minimal photon energy required for an electron transition from the highest occupied state of the emitter (i.e. the VB of $MoTe_2$) to the lowest unoccupied state of the insulator (i.e. the CB of SiO_2). When considering IPE from the semiconductor VB, the density of occupied states below the top VB increases almost linearly, resulting in a value of p equal to 3. The quantum yield can be calculated as $Y = h(\nu)\text{-}(\Phi_e)^3$. Thus, the spectral thresholds for electron IPE can be determined by performing a linear fit of the quantum yield spectra in $Y^{1/3}$ - hν coordinates. To take into account the impact of the image-force barrier lowering (the Schottky effect), the spectral thresholds measured at different externally applied gate bias voltages (Vg) were plotted in Schottky coordinates $\Phi e - \sqrt{F}$ where F is the strength of electric field in SiO_2. These plots are then extrapolated linearly to zero electric field F, which is determined by normalizing Vg to the oxide thickness. This extrapolation allows for the determination of the interface barrier height [41].

CRediT authorship contribution statement

Alessandro Molle: Writing – review & editing, Resources, Funding acquisition. **Alessio Lamperti:** Writing – review & editing, Supervision, Methodology, Conceptualization. **Valeri Afanas'ev:** Writing – review & editing, Validation, Supervision, Resources, Methodology, Data curation. **Gabriele Ferrini:** Writing – review & editing, Supervision. **Pinaka Pani Tummala:** Writing – original draft, Methodology, Investigation, Formal analysis, Data curation, Conceptualization. **Paolo Targa:** Writing – review & editing, Investigation, Formal analysis, Data curation. **Davide Codegoni:** Writing – review & editing, Validation, Resources. **Mario Alia:** Writing – review & editing, Methodology, Data curation. **Andrea Serafini:** Writing – review & editing, Methodology, Investigation, Formal analysis, Data curation. **Christian Martella:** Writing – review & editing.

Declaration of Competing interest

The authors declare the following financial interests/personal relationships which may be considered as potential competing interests: Alessio Lamperti reports financial support was provided by Government of Italy. If there are other authors, they declare that they have no known competing financial interests or personal relationships that could have appeared to influence the work reported in this paper.

Acknowledgements

Financial support from Government of Italy, Ministry of University and Research, PRIN project "PHOTO" grant nr. 2020RPEPNH is acknowledged. Open Access Funding provided by Consiglio Nazionale delle Ricerche within the CRUI-CARE Agreement.

Appendix A. Supporting information

Supplementary data associated with this article can be found in the online version at doi:10.1016/j.elspec.2025.147575.

Data availability

Data will be made available on request.

References

[1] M. Chhowalla, Z. Liu, H. Zhang, Chem. Soc. Rev. 44 (2015) 2584–2586.
[2] X. Yin, C.S. Tang, Y. Zheng, J. Gao, J. Wu, H. Zhang, M. Chhowalla, W. Chen, A.T. S. Wee, Chem. Soc. Rev. 50 (2021) 10087–10115.
[3] B. Qin, M.Z. Saeed, Q. Li, M. Zhu, Y. Feng, Z. Zhou, J. Fang, M. Hossain, Z. Zhang, Y. Zhou, Y. Huangfu, R. Song, J. Tang, B. Li, J. Liu, D. Wang, K. He, H. Zhang, R. Wu, B. Zhao, J. Li, L. Liao, Z. Wei, B. Li, X. Duan, X. Duan, Nat. Comm. 14 (2023) 100164.
[4] B. Koo, G.H. Shin, H. Park, H. Kim, S.Y. Choi, J. Phys. D. Appl. Phys. 51 (2018) 475101.
[5] S. Kim, H. Du, T. Kim, S. Shin, H. kyo Song, H. Kim, D. Kang, C.W. Lee, S. Seo, NPJ 2D Mater. Appl. 4 (2020) 15.
[6] H. Luo, B. Wang, E. Wang, X. Wang, Y. Sun, K. Liu, Crystals 9 (2019) 315.
[7] S. Dissanayake, C. Duan, J. Yang, J. Liu, M. Matsuda, C. Yue, J.A. Schneeloch, J.C. Y. Teo, D. Louca, NPJ Quantum Mater. 4 (2019) 45.
[8] D. Rhodes, D.A. Chenet, B.E. Janicek, C. Nyby, Y. Lin, W. Jin, D. Edelberg, E. Mannebach, N. Finney, A. Antony, T. Schiros, T. Klarr, A. Mazzoni, M. Chin, Y. C. Chiu, W. Zheng, Q.R. Zhang, F. Ernst, J.I. Dadap, X. Tong, J. Ma, R. Lou, S. Wang, T. Qian, H. Ding, R.M. Osgood, D.W. Paley, A.M. Lindenberg, P.Y. Huang, A.N. Pasupathy, M. Dubey, J. Hone, L. Balicas, Nano Lett. 17 (2017) 1616.
[9] H. Kowalczyk, J. Biscaras, N. Pistawala, L. Harnagea, S. Singh, A. Shukla, ACS Nano 17 (2023) 6708–6718.
[10] C.-H. Lee, H. Ryu, G. Nolan, Y. Zhang, Y. Lee, S. Oh, H. Cheong, K. Watanabe, T. Taniguchi, K. Kim, G. Hyoung Lee, P.Y. Huang, Nano Lett. 23 (2023) 677–684.
[11] S. Paul, S. Talukdar, R.S. Singh, S. Saha, Phys. Status Solidi RRL 17 (2023) 2200420.
[12] C. Zhao, J. Huang, Molecules 29 (2024) 5216.
[13] Y. Cheon, S.Y. Lim, K. Kim, H. Cheong, ACS Nano 15 (2021) 2962–2970.
[14] D.H. Keum, S. Cho, J.H. Kim, D.H. Choe, H.J. Sung, M. Kan, H. Kang, J.Y. Hwang, S.W. Kim, H. Yang, K.J. Chang, Y.H. Lee, Nat. Phys. 11 (2015) 482.
[15] T.T. Han, L. Chen, C. Cai, Z.G. Wang, Y.D. Wang, Z.M. Xin, Y. Zhang, Phys. Rev. Lett. 126 (2021) 106602.
[16] C. Ruppert, O.B. Aslan, T.F. Heinz, Nano Lett. 14 (2014) 6231.
[17] N.R. Pradhan, D. Rhodes, S. Feng, Y. Xin, S. Memaran, B.H. Moon, H. Terrones, M. Terrones, L. Balicas, ACS Nano 8 (2014) 5911.
[18] S. Fathipour, N. Ma, W.S. Hwang, V. Protasenko, S. Vishwanath, H.G. Xing, H. Xu, D. Jena, J. Appenzeller, A. Seabaugh, Appl. Phys. Lett. 105 (2014) 192101.
[19] H. Xu, S. Fathipour, E.W. Kinder, A.C. Seabaugh, S.K. Fullerton-Shirey, ACS Nano 9 (2015) 4900.
[20] I.M. Datye, M.M. Rojo, E. Yalon, S. Deshmukh, M.J. Mleczko, E. Pop, Nano Lett. 20 (2020) 1461.
[21] D.Y. Lin, H.P. Hsu, G.H. Liu, T.Z. Dai, Y.T. Shih, Crystals 11 (2021) 964.
[22] L. Sun, M. Ding, J. Li, L. Yang, X. Lou, Z. Xie, W. Zhang, H. Chang, Appl. Surf. Sci. 496 (2019) 143687.
[23] Y. Chen, X. Wang, G. Wu, Z. Wang, H. Fang, T. Lin, S. Sun, H. Shen, W. Hu, J. Wang, J. Sun, X. Meng, J. Chu, Small 14 (2018) 1703293.
[24] C. Martella, E. Kozma, P.P. Tummala, S. Ricci, K.A. Patel, A. Andicsovà-Eckstein, F. Bertini, G. Scavia, R. Sordan, L.G. Nobili, M. Bollani, U. Giovanella, A. Lamperti, A. Molle, Adv. Mater. Interfaces 7 (2020) 2000791.
[25] J. Li, H. Gao, G. Zhou, Y. Li, Y. Chai, G. Hao, J. Appl. Phys. 131 (2022) 110902.
[26] Y. Balaji, Q. Smets, Á. Śzabo, M. Mascaro, D. Lin, I. Asselberghs, I. Radu, M. Luisier, G. Groeseneken, Adv. Funct. Mater. 30 (2020) 1905970.
[27] Y. Balaji, Q. Smets, C.J. Lockhart De La Rosa, A.K.A. Lu, D. Chiappe, T. Agarwal, D. H.C. Lin, C. Huyghebaert, I. Radu, D. Mocuta, G. Groeseneken, IEEE J. Electron Devices Soc. 6 (2018) 1018.
[28] M.K. Jana, A. Singh, A. Sampath, C.N.R. Rao, U.V. Waghmare, Z. Anorg. Allg. Chem. 642 (2016) 1386.
[29] C. Martella, A. Quadrelli, P.P. Tummala, C. Lenardi, R. Mantovan, A. Lamperti, A. Molle, Cryst. Growth Des. 21 (2021) 2970.
[30] P.P. Tummala, S. Ghomi, C.S. Casari, C. Martella, A. Lamperti, A. Molle, Adv. Mater. Interfaces 10 (2023) 2200971.
[31] S. Cho, S. Kim, J.H. Kim, J. Zhao, J. Seok, D.H. Keum, J. Baik, D.-H. Choe, K. J. Chang, K. Suenaga, S.W. Kim, Y.H. Lee, H. Yang, Science 349 (2015) 625.
[32] Y. Chandran, D. Thakur, B. Raju Naik, V. Balakrishnan, Nanotechnology 34 (2023) 375702.
[33] R.J. Powell, J. Appl. Phys. 41 (1970) 2424.
[34] T.A. Empante, Y. Zhou, V. Klee, A.E. Nguyen, I.-H. Lu, M.D. Valentin, S.A. Naghibi Alvillar, E. Preciado, A.J. Berges, C.S. Merida, M. Gomez, S. Bobek, M. Isarraraz, E. J. Reed, L. Bartels, ACS Nano 11 (2017) 900.
[35] V.V. Afanas'ev, G. Delie, M. Houssa, I. Shlyakhov, A. Stesmans, V. Trepalin, J. Phys. Cond. Matter 32 (2020) 413002.
[36] V.V. Afanas'ev, A. Stesmans, J. Appl. Phys. 102 (2007) 081301.
[37] V. Afanas'ev, N. Kolomiiets, M. Houssa, A. Stesmans, Phys. Status Sol. A 215 (2018) 1700865.
[38] J. Kang, S. Tongay, J. Zhou, J. Li, J. Wu, Appl. Phys. Lett. 1 (2013) 102.
[39] I. Shlyakhov, J. Chai, M. Yang, S.J. Wang, V.V. Afanas'Ev, M. Houssa, A. Stesmans, APL Mater. 6 (2017) 026801.
[40] P.P. Tummala, G. Delie, A. Cataldo, S. Ghomi, C. Martella, G. Ferrini, A. Molle, A. Lamperti, V.V. Afanas'ev, Solid State Electron. 209 (2023) 108782.
[41] V.V. Afanas'ev, D. Chiappe, C. Huyghebaert, I. Radu, S. De Gendt, M. Houssa, A. Stesmans, Microelectron. Eng. 147 (2015) 294.